

Unconventional magnetoelectric conductivity and electrochemical response from dipole-like sources of Berry curvature

Ipsita Mandal^{*}

Department of Physics, Shiv Nadar Institution of Eminence (SNIoE),
Gautam Buddha Nagar, Uttar Pradesh 201314, India

We compute longitudinal magnetoelectric conductivity (σ_{zz}) and nonlinear electrochemical response (ECR), applying the semiclassical Boltzmann formalism, for three-dimensional nodal-ring semimetals (vortex nodal-rings and \mathcal{PT} -symmetric nodal-rings) and three-band Hopf semimetals. While the nodal-curves of the former are taken to lie along the $k_z = 0$ -plane, the nodal points of the latter harbour dipoles in their Berry-curvature (BC) profile, with the dipole's axis aligned along the k_z -axis. All these systems are topological and are unified on the aspect that their bands possess a vanishing Chern number. The linear response, σ_{zz} , is obtained from an exact solution when the systems are subjected to collinear electric and magnetic fields applied along the anisotropy axis, viz. \hat{z} . The nonlinear part involves third-rank tensors representing second-order response coefficients, relating the electrical current to the combined effects of the gradient of the chemical potential and an external electric field. We analyse the similarities of the response arising from the vortex nodal-rings and the Hopf semimetals, which can be traced to the dipole-like sources in their BC fields.

CONTENTS

I. Introduction	1
II. Models	3
A. Vortex nodal-ring	3
B. \mathcal{PT} -symmetric nodal-ring	5
C. Three-band Hopf semimetal	5
III. Linear magnetoconductivity for collinear electromagnetic fields	6
A. Vortex nodal-ring	8
B. Three-band Hopf semimetal	8
IV. Nonlinear response coefficients	9
A. Vortex nodal-ring	9
1. Case I: Tilt with respect to k_x -axis	9
2. Case II: Tilt with respect to k_z -axis	10
B. \mathcal{PT} -symmetric nodal-ring	10
1. Case I: Tilt with respect to k_x -axis	10
2. Case II: Tilt with respect to k_z -axis	11
C. Three-band Hopf semimetal	11
1. Case I: Tilt with respect to k_x -axis	11
2. Case II: Tilt with respect to k_z -axis	11
V. Summary and outlook	12
Appendix: Limits of angular integrals for tilted nodal-rings	12
References	12

I. INTRODUCTION

Investigations of transport properties in three-dimensional (3d) semimetals have catapulted into prominence as they often reflect the underlying topological features of the Brillouin zone (BZ). When the BZ harbours symmetry-protected band-crossings in the momentum space (denoted here by $\mathbf{k} \equiv \{k_x, k_y, k_z\}$), the resulting nodal points [1–4] or curves [5, 6] can be characterised by some topological invariant or index. Our efforts are mainly directed at identifying meaningful

* ipsita.mandal@snu.edu.in

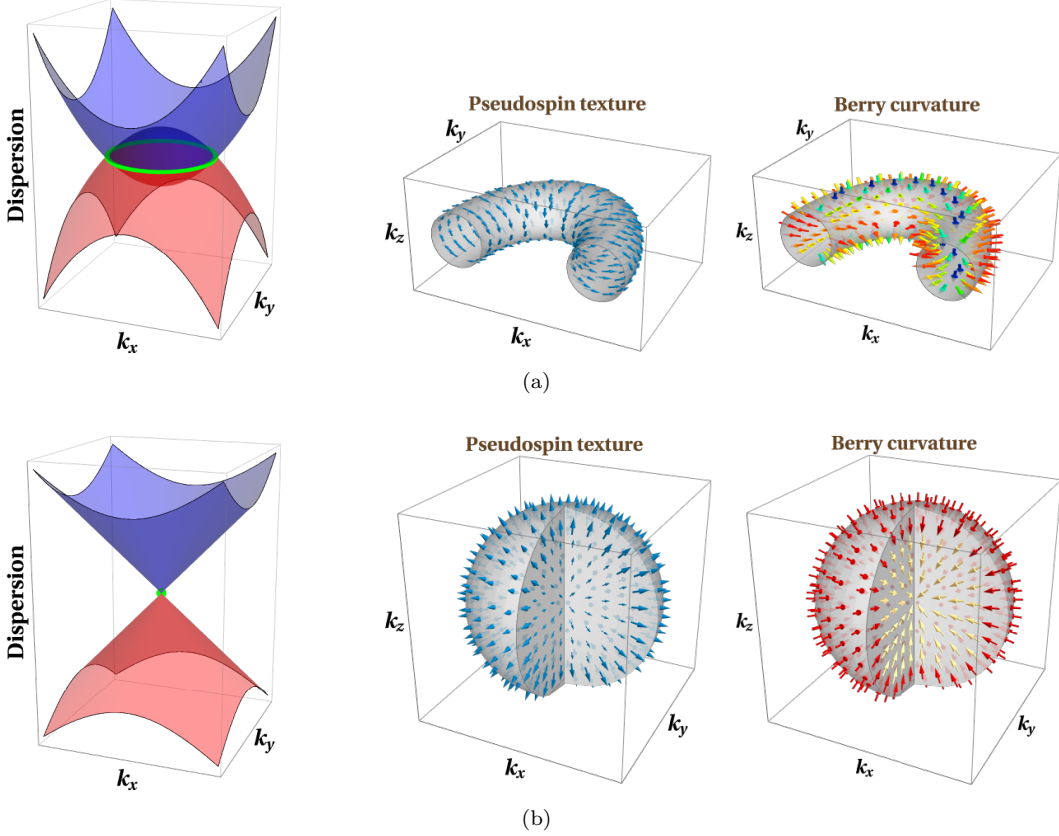


FIG. 1. (a) We show the unique features of a vortex nodal-ring (VRN) in terms of its dispersion against the $k_x k_y$ -plane showing two bands crossing along a circle (highlighted in green), setting $k_z = 0$, and the profile of the vector fields representing the pseudospin and BC. (b) For the sake of comparison with a Weyl node, we show its dispersion (with the green dot denoting the nodal-point), and the pseudospin and BC distributions. The vector fields for each case have been drawn in the vicinity of a section of the Fermi surface for the positive-energy band.

response which will capture this invariant unambiguously. The topological properties often arise as a nontrivial Berry curvature (BC) [7, 8], sourced by the Berry phases of the associated Bloch bands meeting at the nodes of a semimetal. Starting with the pioneering example of the Weyl semimetals (WSMs), the most important telltale signatures of the BC are the intrinsic anomalous-Hall effect [9–11] and the appearance of longitudinal and transverse conductivity in planar-Hall configurations [12–24]. Here, we will focus on a two-band system containing a nodal-loop in the form of a circle [see Fig. 1(a)], thus carrying a representation of the pseudospin-1/2 quantum number (just like the WSMs). Generically, their effective Hamiltonian can be represented as $\mathbf{d}(\mathbf{k}) \cdot \boldsymbol{\sigma}$, where $\boldsymbol{\sigma} = \{\sigma_x, \sigma_y, \sigma_z\}$ is the vector comprising the three Pauli matrices as its three components and defining the 2×2 matrix-operators in the pseudospin space. The 3-component vector \mathbf{d} encodes the pseudospin structure of the two-component spinors representing the two Bloch bands. For a typical nodal-loop protected by \mathcal{PT} -symmetry (where \mathcal{P} and \mathcal{T} represent the operators implementing the inversion and time-reversal symmetries, respectively), has a nonzero BC only along the loop itself, vanishing identically elsewhere.¹ This singular-natured BC is characterised by a nonvanishing Zak phase [24, 25, 33, 34]. However, in the absence of both these symmetries, a different type of nodal-ring may exist, dubbed as the vortex nodal-ring (VNR) [6], which does harbour a nonvanishing nonsingular BC away from the nodal-loop. The nomenclature is related to the fact that the vector field representing $\mathbf{d}(\mathbf{k})$ takes a vortex-like or smoke-ring texture in the momentum space [cf. Fig. 1(a)]. For the ease of reference, we will refer to the other variety of nodal-ring and its gapped cousins (obtained by starting from the \mathcal{PT} -symmetric model) as PTNRs.

The magnitude of the BC-monopole carried by a nodal point is synonymous with the Chern number of any closed 2d surface (in momentum space) containing the node inside, giving us the associated topological invariant in terms of the BC-monopole charge. Beyond this simple picture, we are also now aware of more possibilities of the behaviour of the BC where the nodes act as source of higher-order poles [35–37], which include ideal dipoles, quadrupoles, and so on. They can be thought of the momentum-space analogues of such objects familiar from multipole expansions of electromagnetism. Here, we will consider three-band massless Hopf semimetals which host BC-dipoles.

¹ Adding a mass term of magnitude Δ , for example generated by spin-orbit coupling, makes it gapped. This induces a nonvanishing BC $\propto \Delta$ which happens to have only in-plane components [23–32].

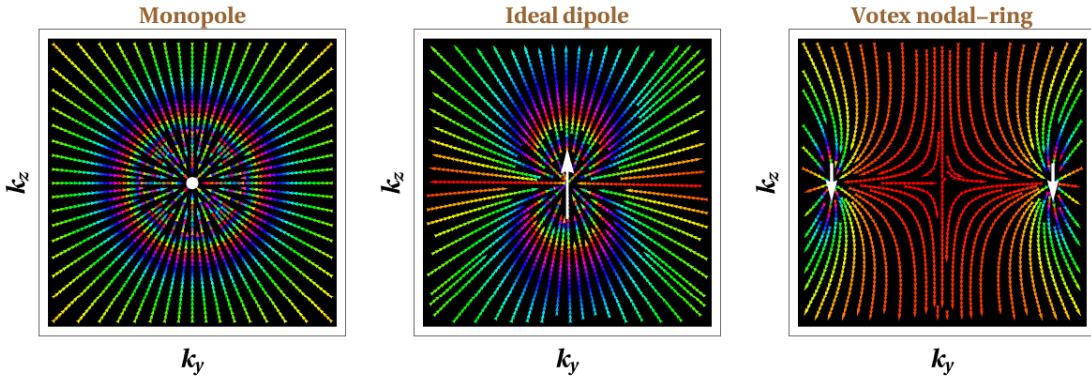


FIG. 2. Profile of the BC-flux distribution for a monopole (e.g., Weyl node), an ideal dipole (e.g., three-band Hopf semimetal) [cf. Eq. (18) with $s = 2$], and a Vortex nodal-ring [cf. Eq. (6) with $s = 2$], projected on the $k_y k_z$ -plane at $k_x = 0$. While the white dot denotes the monopole singularity, the white arrows denote the dipole-like singularities of the BC.

While a non-zero BC-vector field is the first important topological property to affect transport (see Fig. 2 for a comprehensive illustration), it is accompanied by another vector field called the orbital magnetic moment (OMM), sourced by the same Berry phase [7], and also affects transport involving a magnetic field [17–22, 24]. While topology-induced response has been studied quite widely for the PTNRs [23–32], such characteristics have not been explored for the VNRs and BC-dipole nodal points, which we undertake in this paper. In particular, we will perform an analytical computation of the linear magnetoelectric conductivity in planar-Hall set-ups, similar to what was studied in our earlier work involving PTNRs [24]. Such set-ups refer to the application of static and uniform electric (\mathbf{E}) and magnetic (\mathbf{B}) fields, where \mathbf{B} is not necessarily perpendicular to \mathbf{E} .

Nonlinear transport under the effect of an external electric field (or temperature gradient) and the gradient of the chemical potential, constituting a response of electrochemical nature [19]. Here, we dub the associated electrical conductivity tensor as the electrochemical response (ECR). Since the Chern number is zero for the systems under consideration in this paper, some of these coefficients will be zero, unlike nodal-points harbouring BC-monopoles, we will find that there will be nontrivial characterisation of the nontrivial topology by nonzero coefficients in tilted cases.

The paper is organized as follows: In Sec. II, we provide detailed descriptions of the effective models of the nodal-ring and BC-dipole semimetals, whose transport properties we are interested in. Sec. III is devoted to deriving the longitudinal magnetoelectric conductivity for a single VNR or a single BC-dipole nodal point, incorporating exact solutions. We beef up our efforts toward transport-characterisation by considering nonlinear response (in the form of ECR) in Sec. IV. Finally, we end with a summary and outlook in Sec. V. The appendix explains some steps to perform the integrals involving tilted nodal-rings.

All our expressions in the paper are written using the natural units. Basically, this implies that the reduced Planck's constant (\hbar), the speed of light (c), and the Boltzmann constant (k_B) are each set to unity. The magnitude of electric charge, e , has no units and also equals unity in the natural units. However, for tracking the appearance of the electric charge, we will retain e in our expressions.

II. MODELS

In the following three subsections, we describe the three distinct systems we are interested in in this paper.

A. Vortex nodal-ring

The minimal model of a VNR, comprising two bands and a circular nodal-loop lying in the $k_x k_y$ -plane at $k_z = 0$, is captured by [6]

$$\mathcal{H}_0(\mathbf{k}) = \mathbf{d}_0(\mathbf{k}) \cdot \boldsymbol{\sigma} + v_0 \boldsymbol{\eta} \cdot \mathbf{k} \mathbb{I}_{2 \times 2}, \quad \mathbf{d}_0(\mathbf{k}) = \left\{ \frac{-k_x k_z}{m_z}, \frac{-k_y k_z}{m_z}, \frac{k_\perp^2 - k_0^2 - k_z^2}{2m_\perp} \right\}, \quad k_\perp = \sqrt{k_x^2 + k_y^2},$$

$$\boldsymbol{\eta} = \{\eta_x, \eta_y, \eta_z\}. \quad (1)$$

where k_0 , m_z , and m_\perp are material-dependent parameters. At the $k_z = 0$ plane, the two bands cross at $k_\perp = k_0$, defining a nodal-ring of radius k_0 . Therefore, $v_z \equiv k_0/m_z$ and $v_\perp \equiv k_0/m_\perp$ encode the values of the Fermi velocities perpendicular and parallel to the nodal plane, respectively. In the following, we will set $v_z = v_\perp = v_0$ for the sake of simplicity. We have also included a generic tilting term, $v_0 \boldsymbol{\eta} \cdot \mathbf{k}$.

For low-energy excitations confined in the vicinity of the resulting Fermi surface, the dominant transport-signatures of the low-energy quasiparticles can be captured by a linearised Hamiltonian, \mathcal{H} . It comprises terms which deviate only at linear-order-in-momentum from the location of the nodal line [24, 38]. This can be accomplished by implementing a transformation to the cylindrical coordinates as follows:

$$k_x = k_{\perp} \cos \phi, \quad k_y = k_{\perp} \sin \phi, \quad k_{\perp} = k_0 + \kappa_{\perp}. \quad (2)$$

Clearly, $\kappa_{\perp} \in [-k_0, \infty)$. However, for the low-energy processes we are interested in, we must have $|\kappa_{\perp}| \ll k_0$, as k_0 acts as an ultraviolet-energy scale. Subsequently, linearising in the small-valued variables (viz. κ_{\perp} and k_z), we end up with

$$\mathcal{H}_{vn}(\mathbf{k}) = \mathbf{d}_{vn}(\mathbf{k}) \cdot \boldsymbol{\sigma} + v_0 \boldsymbol{\eta} \cdot \mathbf{k} \mathbb{I}_{2 \times 2}, \quad \mathbf{d}_{vn}(\mathbf{k}) = v_0 \{-k_z \cos \phi, -k_z \sin \phi, \kappa_{\perp}\}. \quad (3)$$

For the linearised Hamiltonian \mathcal{H} , the eigenvalues of the two bands are obtained as

$$\varepsilon_s(\mathbf{k}) = (-1)^s \epsilon_k + v_0 \boldsymbol{\eta} \cdot \mathbf{k}, \quad \epsilon_k = v_0 \sqrt{\kappa_{\perp}^2 + k_z^2}, \quad s \in \{1, 2\}. \quad (4)$$

The band-velocities of the quasiparticles are given by

$$\mathbf{v}^{(0,s)}(\mathbf{k}) \equiv \nabla_{\mathbf{k}} \varepsilon_s(\mathbf{k}) = \frac{(-1)^s v_0^2}{\epsilon_k} \{\kappa_{\perp} \cos \phi, \kappa_{\perp} \sin \phi, k_z\} + v_0 \boldsymbol{\eta}. \quad (5)$$

The Berry curvature (BC) and the orbital magnetic moment (OMM), associated with the s^{th} band, turn out to be

$$\boldsymbol{\Omega}_s(\mathbf{k}) = \frac{(-1)^{s+1} v_0^3 k_z}{2(k_0 + \kappa_{\perp}) \epsilon_k^3} \{\kappa_{\perp} \cos \phi, \kappa_{\perp} \sin \phi, k_z\}, \quad \mathbf{m}(\mathbf{k}) = \frac{-e v_0^3 k_z}{2(k_0 + \kappa_{\perp}) \epsilon_k^2} \{\kappa_{\perp} \cos \phi, \kappa_{\perp} \sin \phi, k_z\}. \quad (6)$$

See Fig. 2(b) for a depiction of the cross-section of the BC profile in the $k_x = 0$ plane. The OMM behaves exactly like the electron's spin because, on applying a magnetic field (\mathbf{B}), it couples to it through a Zeeman-like term. Therefore, the shift in energy caused by the OMM is captured by

$$\varepsilon_m(\mathbf{k}) = \frac{e v_0^3 k_z (B_x \kappa_{\perp} \cos \phi + B_y \kappa_{\perp} \sin \phi + B_z k_z)}{2 \epsilon_k^2 (k_0 + \kappa_{\perp})}. \quad (7)$$

The OMM-induced parts are the same for both the bands and, hence, we have not attached any s index to them. The BC can be imagined to be caused by a continuous distribution of ideal dipoles along the nodal-ring, as see from Figs. 2(c) and 1(a).

We will work in the $T \rightarrow 0$ limit, such that the Fermi-Distribution function, denoted as $f_0(\mathcal{E})$ for a band with dispersion E , goes to $\Theta(\mu - \mathcal{E})$. Hence, its derivative with respect to \mathcal{E} goes as $\partial_{\mathcal{E}} f_0 \rightarrow -\delta(\mathcal{E} - \mu)$. We will use the shorthand-notation of $\int_{\mathbf{k}} \cdots \equiv \int \frac{d^3 \mathbf{k}}{(2\pi)^3} \cdots$ for the \mathbf{k} -integrals. While performing these integrals, we will resort to using the toroidal coordinates, defined as follows:

$$k_x = (k_0 + \kappa_{\perp}) \cos \phi, \quad k_y = (k_0 + \kappa_{\perp}) \sin \phi, \quad k_z = \kappa \sin \gamma, \quad \kappa_{\perp} \equiv \kappa \cos \gamma = k_{\perp} - k_0. \quad (8)$$

The Jacobian of the transformation is given by

$$J = \kappa k_{\perp}. \quad (9)$$

In terms of the toroidal coordinates, k_0 represents the major radius (i.e., the distance between a point on the nodal-ring and the center of the torus), κ denotes the minor radius (i.e., the radius of the cross-section of the torus). The angular coordinates, ϕ and γ , span over $\in [0, 2\pi]$, representing rotation around the torus's axis of revolution and rotation around the centre of a cross-section, respectively. In our calculations for conductivity, we will consider applying a non-negative value of the chemical potential, μ . Therefore, for $\eta = 0$, only the $s = 2$ band will contribute.

For the tilted case, some extra care needs to be taken. When the tilting is with respect to the $k_x k_y$ -plane, the ring-toroid structure can get drastically modified. Let us choose this in-plane tilting with respect to the k_x -axis, without any loss of generality. Depending on the relative values of μ and $\tilde{\eta} \equiv v_0 k_0 \eta_x$. For nonzero $\tilde{\eta}$, there are several possibilities [39] corresponding to (a) ring-cyclide: $0 < \tilde{\eta} < \mu$; (b) horn-cyclide formed from the $s = 2$ band only: $\mu > 0$ and $\tilde{\eta} = \mu$; (c) symmetric horn-cyclide formed by both the bands: $\mu = 0$ and $\tilde{\eta} > 0$; and (d) (asymmetric) horn-cyclide formed by both the bands: $0 < \mu < \tilde{\eta}$. For visual aid, Fig. 3 depicts the ϕ -dependence of these distinct-shaped cyclides. In the language of Eqs. (2) and (8), we have $\epsilon_k = v_0 \kappa$ and

$$\delta(\varepsilon_s - \mu) \equiv \delta\left((-1)^s v_0 \kappa + \eta v_0 (k_0 + \kappa \cos \gamma) \cos \phi - \mu\right) = \frac{\delta\left(\kappa - \frac{\mu - \tilde{\eta} \cos \phi}{v_0 \zeta_s}\right)}{v_0 |\zeta_s|},$$

where $\zeta_s = (-1)^s + \eta \cos \gamma \cos \phi$ and $\tilde{\eta} = \eta v_0 k_0$. (10)

Depending on the relative values of μ and $\tilde{\eta}$, both the bands may contribute, and the valid range of ϕ is determined from the points where the Fermi-momentum vanishes, viz. $\kappa = 0 \Rightarrow \cos \phi = \mu/\tilde{\eta}$. More details can be found in the appendix.

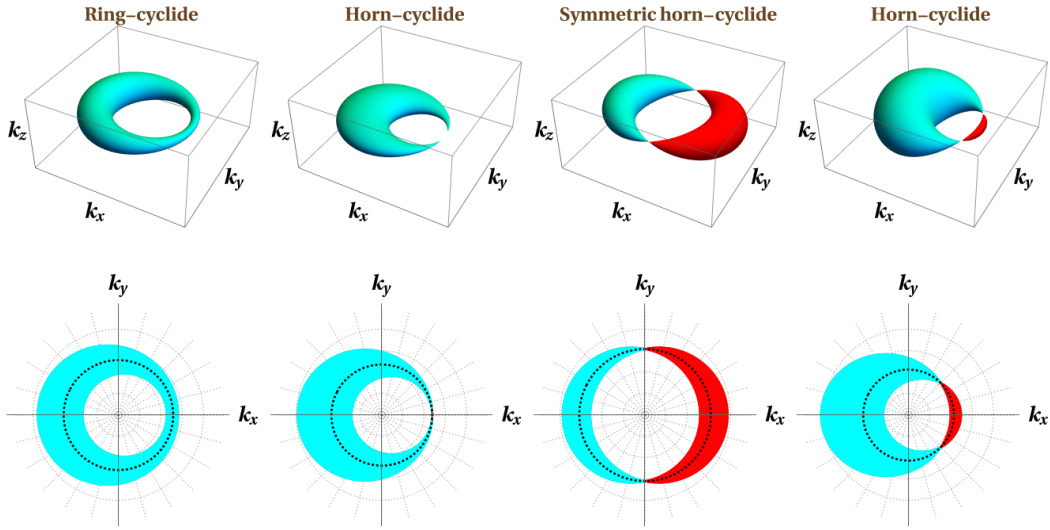


FIG. 3. On introducing tilt, the Fermi surfaces take the forms of different kinds of cyclides, which depend on the values of μ and ηk_0 . The red and cyan colours depict the $s = 1$ and $s = 2$ bands, respectively. While (a) illustrates the full 2d Fermi surfaces, (b) shows the corresponding projections on the $k_x k_y$ -plane for $k_z = 0$. The dotted black circle represents the original VNR at $\mu = \eta = 0$ for the sake of reference.

B. \mathcal{PT} -symmetric nodal-ring

The minimal model of a two-band ideal nodal-ring of the PTNR variety, lying in the $k_x k_y$ -plane, and linearised in momenta about the nodal-circle, is captured by [5, 24, 26]

$$\mathcal{H}_{pt}(\mathbf{k}) = \mathbf{d}_{pt}(\mathbf{k}) \cdot \boldsymbol{\sigma} + v_0 \boldsymbol{\eta} \cdot \mathbf{k} \mathbb{I}_{2 \times 2}, \quad \mathbf{d}_{pt}(\mathbf{k}) = \{v_0 (k_{\perp} - k_0), v_z k_z, 0\}. \quad (11)$$

For the sake of simplicity, we will set $v_z = v_0$. The eigenenergies and the band-velocities take the same forms as the VRN, viz. Eqs. (4) and (5).

Unlike the VNR model, the PTNR has a vanishing BC everywhere for each band, except at the nodal-ring. It can be parametrised as [25, 40]

$$\boldsymbol{\Omega}_s(\mathbf{k}) = (-1)^{s+1} \pi \delta(k_z) \delta(k_{\perp} - k_0) \hat{\phi} = (-1)^{s+1} \pi \delta(k_z) \delta(\kappa_{\perp}) \{-\sin \phi, \cos \phi, 0\}, \quad (12)$$

where it becomes singular. Here, $\hat{\phi}$ denotes the unit vector along the ϕ -coordinate. Similarly, the OMM is singular at the nodal-ring, expressed as

$$\mathbf{m}(\mathbf{k}) = e (-1) v_0 \kappa \pi \delta(\kappa \sin \gamma) \delta(\kappa \cos \gamma) \hat{\phi} = -e v_0 \kappa \pi \frac{\delta(\gamma)}{\kappa |\cos \gamma|} \frac{\delta(\kappa)}{|\cos \gamma|} \hat{\phi} = -e v_0 \pi \delta(\kappa) \delta(\gamma) \hat{\phi}. \quad (13)$$

For evaluating some the conductivity expressions, we will need to use the expression of the cross-product of a vector, \mathbf{A} , with $\boldsymbol{\Omega}_s$. This turns out to be

$$\mathbf{A} \times \boldsymbol{\Omega}_s(\mathbf{k}) = (-1)^{s+1} \pi \delta(k_z) \delta(k_{\perp} - k_0) \hat{\mathbf{e}}_{\phi} = (-1)^s \pi \delta(k_z) \delta(k_{\perp} - k_0) \{A_z \cos \phi, A_z \sin \phi, -A_x \cos \phi - A_y \sin \phi\}. \quad (14)$$

C. Three-band Hopf semimetal

Hopf semimetals hosting nodal-points which host BC-dipoles, rather than monopoles, were introduced in Ref. [35] multifold Hopf semimetals (MMHSs) have been introduced which host BC-dipoles at nodes where linearly-dispersing bands cross. We consider the simplest case with threefold-degenerate node, captured by the effective continuum Hamiltonian [35, 36],

$$H_h = v_0 (k_x \lambda_1 + k_y \lambda_2 + k_z \lambda_5 + \boldsymbol{\eta} \cdot \mathbf{k} \mathbb{I}_{3 \times 3}), \quad (15)$$

where

$$\lambda_1 = \begin{bmatrix} 0 & 1 & 0 \\ 1 & 0 & 0 \\ 0 & 0 & 0 \end{bmatrix}, \quad \lambda_2 = \begin{bmatrix} 0 & -i & 0 \\ i & 0 & 0 \\ 0 & 0 & 0 \end{bmatrix}, \quad \lambda_5 = \begin{bmatrix} 0 & 0 & -i \\ 0 & 0 & 0 \\ i & 0 & 0 \end{bmatrix}. \quad (16)$$

We have added a tilt term to see its effect in nonlinear response. The system comprises three bands, with eigenvalues

$$\varepsilon_s(\mathbf{k}) = \begin{cases} (-1)^s v_0 k + v_0 \boldsymbol{\eta} \cdot \mathbf{k} & \text{for } s \in \{1, 2\} \\ v_0 \boldsymbol{\eta} \cdot \mathbf{k} & \text{for } s = 0 \end{cases}. \quad (17)$$

The value $s = 0$ represents a nondispersive flat-band for no tilt, which does not contribute to transport. Using an orthonormal set of eigenvectors, the BC and the OMM are obtained as

$$\boldsymbol{\Omega}_s(\mathbf{k}) = \begin{cases} \frac{k_z \mathbf{k}}{k^4} & \text{for } s = 1, 2 \\ \frac{-2 k_z \mathbf{k}}{k^4} & \text{for } s = 0 \end{cases} \quad \text{and} \quad \mathbf{m}_s(\mathbf{k}) = \begin{cases} \frac{(-1)^{s+1} e k_z \mathbf{k}}{k^3} & \text{for } s = 1, 2 \\ 0 & \text{for } s = 0 \end{cases}, \quad (18)$$

respectively. See Fig. 2(c) for a depiction of the cross-section of the BC profile in the $k_x = 0$ plane.

While performing various integrals for the BC-dipole system, we will resort to using the usual spherical-polar coordinates, defined as follows:

$$k_x = k \sin \gamma \cos \phi, \quad k_y = k \sin \gamma \sin \phi, \quad k_z = k \cos \gamma. \quad (19)$$

We note that, here, $\gamma \in [0, \pi]$, unlike the toroidal coordinates.

III. LINEAR MAGNETOCONDUCTIVITY FOR COLLINEAR ELECTROMAGNETIC FIELDS

In this section, we will compute the magnetoelectric conductivity adopting the methodology of semiclassical Boltzmann formalism [7, 16, 18, 19, 21, 41, 42], considering collinear electric ($\mathbf{E} = E \hat{\mathbf{z}}$) and magnetic ($\mathbf{B} = B \hat{\mathbf{z}}$) fields. In particular, we will not limit ourselves to the relaxation-time formalism and use the exact solutions, which have been applied already for various nodal-point semimetals successfully [21, 22]. Hence, we do not repeat the derivation of the main formula, of which one can find very detailed explanations in those earlier works. Instead, we start with the *linearised Boltzmann equation*

$$w_{\chi,s}^z(\mathbf{k}) + e B [\boldsymbol{\Omega}_{\chi,s}(\mathbf{k}) \cdot \mathbf{w}_{\chi,s}(\mathbf{k})] - e B [\mathbf{w}_{\chi,s}(\mathbf{k}) \times \hat{\mathbf{z}}(\mathbf{k})] \cdot \nabla_{\mathbf{k}} \Lambda_{\chi,s}^z(\mathbf{k}) = \mathcal{D}_{\chi,s}^{-1}(\mathbf{k}) \sum_{\tilde{\chi}, \tilde{s}} \int_{\mathbf{k}'} \mathcal{M}_{s,\tilde{s}}^{\chi,\tilde{\chi}}(\mathbf{k}, \mathbf{k}') [\Lambda_{\tilde{\chi}, \tilde{s}}^z(\mathbf{k}') - \Lambda_{\chi,s}^z(\mathbf{k})], \quad (20)$$

whose solution gives us the conductivity. The symbol $\int_{\mathbf{k}} \equiv \int d^3 \mathbf{k} \mathcal{D}_{\tilde{\chi}, \tilde{s}}^{-1}(\mathbf{k}) / (2\pi)^3$ stands for the three-dimensional integral in the momentum space, containing the modified phase-space factor due to the BC. Here, an index χ has been included to take into account systems with nodal-points with a dependence on the chirality. The various symbols appearing in the equation are explained below:

1. The phase-space volume element for the quasiparticles occupying a Bloch band gets modified by a nonzero BC via the factor of $[\mathcal{D}_{\chi,s}(\mathbf{k})]^{-1}$, where

$$\mathcal{D}_{\chi,s}(\mathbf{k}) = [1 + e \{ \mathbf{B} \cdot \boldsymbol{\Omega}_{\chi,s}(\mathbf{k}) \}]^{-1}. \quad (21)$$

2. A nonzero OMM gives rise to a Zeeman-like correction to the bare dispersion [7] in the presence of a magnetic field, modifying it to

$$\xi_{\chi,s}(\mathbf{k}) = \varepsilon_s(\mathbf{k}) + \varepsilon_{\chi,s}^{(m)}(\mathbf{k}), \quad \varepsilon_{\chi,s}^{(m)}(\mathbf{k}) = -\mathbf{B} \cdot \mathbf{m}_{\chi,s}(\mathbf{k}). \quad (22)$$

This, in turn, modifies the group-velocity as

$$\mathbf{w}_{\chi,s}(\mathbf{k}) \equiv \nabla_{\mathbf{k}} \xi_{\chi,s}(\mathbf{k}) = \mathbf{v}_s(\mathbf{k}) + \mathbf{v}_{\chi,s}^{(m)}(\mathbf{k}), \quad \mathbf{v}_{\chi,s}^{(m)}(\mathbf{k}) = \nabla_{\mathbf{k}} \varepsilon_{\chi,s}^{(m)}(\mathbf{k}). \quad (23)$$

The effects of OMM show up via the modified energy appearing in the equilibrium Fermi-Dirac distribution, $f_0(\xi_{\chi,s}(\mathbf{k}), \mu, T) = [1 + \exp\{(\xi_{\chi,s}(\mathbf{k}) - \mu) / T\}]^{-1}$, where T is the temperature. While using f_0 in various equations, we will be suppressing its μ - and T -dependence for uncluttering of notations. Moreover, in what follows, we will restrict our calculations to the $T = 0$ limit.

3. $I_{\text{coll}}[f_{\chi,s}(\mathbf{k})]$ symbolises the so-called *collision integral*, which comprises the relevant scattering processes trying to relax $f_{\chi,s}(\mathbf{k})$ towards $f_0(\xi_{\chi,s}(\mathbf{k}))$. For point-scattering mechanisms,

$$I_{\text{coll}}[f_{\chi,s}(\mathbf{k})] = \sum_{\tilde{\chi}, \tilde{s}} \int_{\mathbf{k}'} \mathcal{M}_{s,\tilde{s}}^{\chi,\tilde{\chi}}(\mathbf{k}, \mathbf{k}') [f_{\tilde{\chi}, \tilde{s}}(\mathbf{k}') - f_{\chi,s}(\mathbf{k})], \quad (24)$$

where $\int_k \equiv \int d^3\mathbf{k} \mathcal{D}_{\tilde{\chi},\tilde{s}}^{-1}(\mathbf{k})/(2\pi)^3$ denotes the three-dimensional integral in the momentum space, containing the modified phase-space factor due to the BC. Furthermore, elastic and pseudospin-independent scatterings, we have the simple expression of

$$\mathcal{M}_{s,\tilde{s}}^{\chi,\tilde{\chi}}(\mathbf{k}, \mathbf{k}') = \frac{2\pi \rho_{\text{imp}} |\mathcal{V}_{s,\tilde{s}}^{\chi,\tilde{\chi}}|^2}{V} \left| \{\psi_{\tilde{\chi},\tilde{s}}(\mathbf{k}')\}^\dagger \psi_{\chi,s}(\mathbf{k}) \right|^2 \delta(\xi_{\tilde{\chi},\tilde{s}}(\mathbf{k}') - \xi_{\chi,s}(\mathbf{k})). \quad (25)$$

Here, ρ_{imp} represents the impurity-concentration (acting as the scattering centres), V denotes the system's volume, and $|\mathcal{V}_{s,\tilde{s}}^{\chi,\tilde{\chi}}|^2$ stands for the scattering-strength (which in general parametrise intraband, interband, intranode, and internode processes).

4. We have parametrised the deviation of the quasiparticle-distribution from the equilibrium as

$$\delta f_{\chi,s}(\mathbf{k}) = -e \frac{\partial f_0(\xi_{\chi,s}(\mathbf{k}))}{\partial \xi_{\chi,s}(\mathbf{k})} E \Lambda_{\chi,s}^z(\mathbf{k}),$$

where $\Lambda_{\chi,s}(\mathbf{k})$ is the vectorial mean-free path. For our configuration, we get a nontrivial equation only for the z -component of $\Lambda_{\chi,s}(\mathbf{k})$, viz. $\Lambda_{\chi,s}^z(\mathbf{k})$.

To solve the integro-differential equation represented by Eq. (20), we take the self-consistent ansatz [21] that $\Lambda_{\chi,s}^z \equiv \Lambda_{\chi,s}^z(\mu, \gamma)$ at an energy μ , which only depends on the polar angle, γ , and the chemical potential, μ . This is because, for elastic scatterings, the integral over the full momentum space can be replaced by an integral over the Fermi surface at energy $\xi_{\chi,s}(\mathbf{k}) = \mu$, and the dependence on ϕ should not be there because of the rotational symmetry of the entire system in the $k_x k_y$ -plane. Consequently, the momentum-space integrals reduce to the respective Fermi surfaces at energy $\xi_{\chi,s}(k_F^{\chi,s}, \gamma) = \mu$ with T set to zero, denoted by the set of Fermi momenta, $\{k_F^{\chi,s}(\gamma)\}$. The self-consistency can be easily checked from the fact that $[\Omega_s^\chi(\mathbf{k}) \cdot \mathbf{w}_{\chi,s}(\mathbf{k})]$ is ϕ -independent and $[\mathbf{w}_{\chi,s}(\mathbf{k}) \times \hat{\mathbf{z}}] \cdot \nabla_{\mathbf{k}} \Lambda_{\chi,s}^z(\mu, \gamma)$ evaluates to zero. Thus, although the spinor overlaps might depend on ϕ and ϕ' , they will drop out on performing the integrations over these angles. Hence, we will use a ϕ - and ϕ' -integrated overlap function, $\mathcal{T}_{s,\tilde{s}}^{\chi,\tilde{\chi}}(\gamma, \gamma')$. Defining

$$\tau_{\chi,s}^{-1}(\mu, \theta) = \sum_{\tilde{\chi}, \tilde{s}} V \int_{\mathbf{k}'} \mathcal{M}_{s,\tilde{s}}^{\chi,\tilde{\chi}}(\mathbf{k}, \mathbf{k}'), \quad h_{\chi,s}(\mu, \theta) = \mathcal{D}_{\chi,s}(\mathbf{k}) [w_{\chi,s}^z(\mathbf{k}) + e B \{\Omega_{\chi,s}(\mathbf{k}) \cdot \mathbf{w}_{\chi,s}(\mathbf{k})\}], \quad (26)$$

Eq. (20) further reduces to

$$h_{\chi,s}(\mu, \gamma) + \frac{\Lambda_{\chi,s}^z(\mu, \gamma)}{\tau_{\chi,s}(\mu, \gamma)} = \sum_{\tilde{\chi}, \tilde{s}} \frac{\rho_{\text{imp}} |\mathcal{V}_{s,\tilde{s}}^{\chi,\tilde{\chi}}|^2}{2\pi} \int d\gamma' \frac{\mathcal{J}(\mathbf{k}') \mathcal{D}_{\tilde{\chi},\tilde{s}}^{-1}(\mathbf{k}')}{|\hat{\mathbf{k}}' \cdot \nabla_{\mathbf{k}'} \xi_{\chi,s}(\mathbf{k}')|} \mathcal{T}_{s,\tilde{s}}^{\chi,\tilde{\chi}}(\gamma, \gamma') \Lambda_{\tilde{\chi},\tilde{s}}^z(\mu, \gamma') \Big|_{k' = k_F^{\tilde{\chi},\tilde{s}}}. \quad (27)$$

The factor \mathcal{J} arises as the Jacobian for switching to the toroidal or spherical-polar coordinates, depending on whether we are dealing with the nodal-rings or BC-dipole nodal-point. The part $|\hat{\mathbf{k}}' \cdot \nabla_{\mathbf{k}'} \xi_{\chi,s}(\mathbf{k}')|^{-1}$ arises from converting $\delta(\xi_{\tilde{\chi},\tilde{s}}(\mathbf{k}') - \mu)$ to $\delta(\kappa' - k_F^{\tilde{\chi},\tilde{s}})$ (for the nodal-rings) or $\delta(k' - k_F^{\tilde{\chi},\tilde{s}})$ (for the nodal points), with $k_F^{\chi,s}$ parametrising the radius of the Fermi surface as measured from the gapless ring (i.e., the locus of the band-touching curve) or the band-touching point. As a final step to solve the still complicated-looking integro-differential equation is to parametrise $\Lambda_{\chi,s}^z(\mu, \gamma)$ by a meaningful ansatz. Basically, the ansatz must ensure that $\Lambda_{\chi,s}^z(\mu, \gamma) \Lambda_{\tilde{\chi},\tilde{s}}^z(\mu, \gamma')$ contains all sinusoidal terms appearing in $\mathcal{T}_{s,\tilde{s}}^{\chi,\tilde{\chi}}(\gamma, \gamma')$, which will depend on the eigenspinors of the respective systems. The conductivity is then determined by the expression,

$$\sigma_{zz} = -\frac{e^2}{V} \sum_{\chi,s} \int \frac{d^3\mathbf{k}}{(2\pi)^3} [w_{\chi,s}^z(\mathbf{k}) + e B \{\Omega_{\chi,s}(\mathbf{k}) \cdot \mathbf{w}_{\chi,s}(\mathbf{k})\}] \delta(\xi_{\chi,s}(\mathbf{k}) - \mu) \Lambda_{\chi,s}^z(\mu, \gamma). \quad (28)$$

In the following subsections, we will discuss the features of the quantity,

$$\delta\sigma_{zz} \equiv \sigma_{zz}(B)/\sigma_{xx}(B=0) - 1, \quad (29)$$

obtained through numerics. We will consider the features for a single VNR and a single BC-dipole, which feature nonzero BC and OMM without introducing a gap (unlike the PTNR). Thus, we will drop the index χ in what follows. For each case, on applying a chemical potential $\mu > 0$, only the $s = 2$ band will participate in transport, which means only $|\mathcal{V}_{2,2}|^2$ matters (caused by intraband-scattering processes), which we parametrise as

$$|\mathcal{V}_{2,2}|^2 = \frac{2\pi}{\rho_{\text{imp}}} \beta_{\text{intr}}. \quad (30)$$

We vary μ and show the behaviour in Fig. 4 for two different values (with β_{intr} set to unity). The two curves represent scenarios when the linear-in- B and the quadratic-in- B terms dominate, respectively.

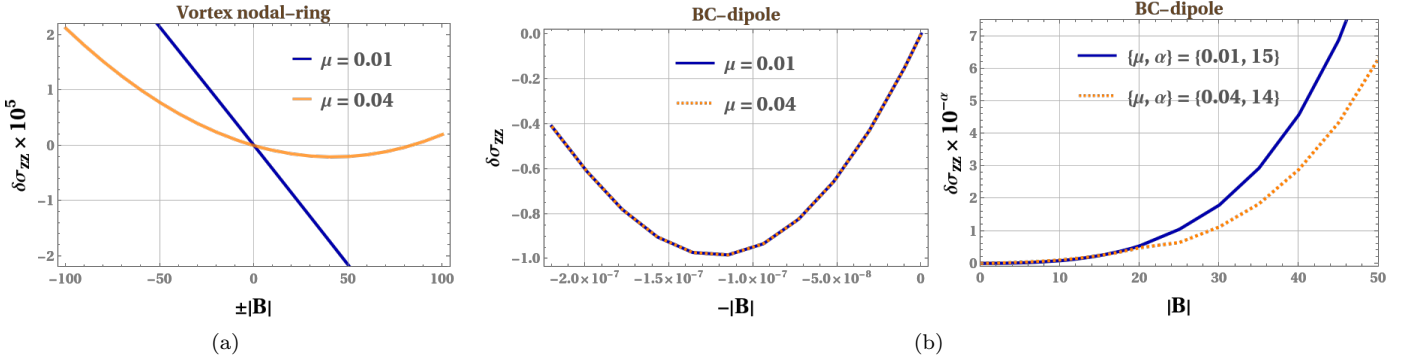


FIG. 4. Behaviour of $\delta\sigma_{zz}$ as a function of $B_z = \pm|\mathbf{B}|$ (in eV 2), setting $v_0 = 0.0004$ and $\beta_{\text{intr}} = 1$. We have shown the curves for two different values of μ , viz. $\mu = 0.01$ eV and $\mu = 0.04$ eV. While subfigure (a) represent the characteristics of a VNR, subfigure (b) depicts the response of a BC-dipole.

A. Vortex nodal-ring

Using the eigenspinors of the tiltless Hamiltonian of Eq. (3), the overlap-function for a single node turns out to be

$$\mathcal{T}_{2,2}(\gamma, \gamma') = \frac{1 + \cos \gamma \cos \gamma'}{2}. \quad (31)$$

This dictates the ansatz,

$$\Lambda_2^z(\mu, \gamma) = \tau_2(\mu, \gamma) [-h_2(\mu, \gamma) + \lambda + a \cos \gamma], \quad (32)$$

corresponding to the positive-energy band. This leaves us with the problem of solving for the 2 unknown coefficients, $\{\lambda, a\}$. Plugging in the ansatz in Eq. (27) furnishes the linear equations, which can be written as a matrix equation of the form

$$\mathcal{AC} = \mathcal{H}, \text{ where } \mathcal{C} = [\lambda \ a]^T. \quad (33)$$

Additionally, the electron-number conservation furnishes the constraint of $\int_k \delta f_2(\mathbf{k}) = 0$. Fig. 4(a) illustrates the conductivity behaviour setting $v_0 = 0.0004$ and $\beta_{\text{intr}} = 1$. The curves indicate the presence of both linear-in- $|\mathbf{B}|$ and quadratic-in- $|\mathbf{B}|$ terms.

B. Three-band Hopf semimetal

Using the eigenspinors of the tiltless Hamiltonian of Eq. (15), the overlap-function for a single node turns out to be

$$\mathcal{T}_{2,2}(\gamma, \gamma') = \frac{3 + 4 \cos \gamma \cos \gamma' + \cos(2\gamma) \cos(2\gamma')}{8}. \quad (34)$$

This dictates the ansatz,

$$\Lambda_2^z(\mu, \gamma) = \tau_2(\mu, \gamma) [-h_2(\mu, \gamma) + \lambda + a \cos \gamma + b \cos(2\gamma)], \quad (35)$$

corresponding to the positive-energy band. This leaves us with the problem of solving for the 3 unknown coefficients, $\{\lambda, a, b\}$. Plugging in the ansatz in Eq. (27) furnishes the linear equations, which can be written as a matrix equation of the form

$$\mathcal{AC} = \mathcal{H}, \text{ where } \mathcal{C} = [\lambda \ a \ b]^T. \quad (36)$$

Additionally, the electron-number conservation furnishes the constraint of $\int_k \delta f_2(\mathbf{k}) = 0$. Fig. 4(b) illustrates the conductivity behaviour setting $v_0 = 0.0004$ and $\beta_{\text{intr}} = 1$. The curves indicate the presence of both linear-in- $|\mathbf{B}|$ and quadratic-in- $|\mathbf{B}|$ terms. For \mathbf{B} directed along the negative z -axis, since the equation of the Fermi momentum is obtained as $k_F = 2\mu v_0/(e B_z \cos^2 \gamma + 2v_0^2)$, we must have $2v_0^2 > e|B_z|$. Hence, the valid regime for negative B_z has been shown separately in Fig. 4(b).

IV. NONLINEAR RESPONSE COEFFICIENTS

In this section, we will focus on computing a nonlinear response in the form of the ECR. Contrary to σ_{zz} computed in Sec. III, here we will restrict ourselves to the relaxation-time approximation since the exact method will be challenging to implement and solve for the purpose of computing the ECR. The main purpose of computing the associated response coefficients is to shed light on how the anisotropic BC shows up in transport, despite the Chern number being zero in the systems under study.

The reader is referred to Ref. [19] for a detailed derivation of the forms of the electric current density, denoted by \mathbf{J}_s and \mathbf{J}_s^{th} , respectively, starting from the Boltzmann equations (which we do not repeat here). The final expressions are obtained by solving for $\delta f_s(\mathbf{r}, \mathbf{k})$, which is the deviation of the distribution of the quasiparticles from the equilibrium, upto second order in ϵ . Here, $\epsilon \in [0, 1]$ is a perturbative parameter, which quantifies the smallness of the magnitude of the probe fields which usually comprise \mathbf{E} , $\nabla_{\mathbf{r}}T$, and $\nabla_{\mathbf{r}}\mu$. In other words, we work in the regime where $|\mathbf{E}| \propto \epsilon$, $|\nabla_{\mathbf{r}}T| \propto \epsilon$, and $|\nabla_{\mathbf{r}}\mu| \propto \epsilon$, and use the expression,

$$f_s(\mathbf{r}, \mathbf{k}) = f_0(\varepsilon_s) + \epsilon f_s^{(1)}(\varepsilon_s) + \epsilon^2 f_s^{(2)}(\varepsilon_s) + \mathcal{O}(\epsilon^3), \quad (37)$$

in a perturbative expansion in ϵ . Finally, we set $\epsilon = 1$ at the end of our computations.

For computing the ECR, we set \mathbf{B} and $\nabla_{\mathbf{r}}T$ to zero. The part of the total electrical current density (\mathbf{J}_s), which shows a quadratic dependence on the probe fields \mathbf{E} and $\nabla_{\mathbf{r}}\mu$, is denoted by $\bar{\mathbf{J}}^s$. This is the electrochemical current density, with its components being proportional to the quadratic combinations of the form $E_a \partial_b \mu$. Its a^{th} components is given by

$$\bar{\mathbf{J}}_a^s = \vartheta_{abc}^s \partial_b \mu E_c, \quad (38)$$

where ϑ_{abc}^s is a rank-three conductivity tensor for the s^{th} band. Since the dependence of the electric current on the probe fields is at second order, we call the resulting response to be nonlinear. We divide it up as

$$\bar{\mathbf{J}}^s = \mathbf{J}^{(s,1)} + \mathbf{J}^{(s,2)}, \quad \vartheta_{abc}^s = \vartheta_{abc}^{(s,1)} + \vartheta_{abc}^{(s,2)}, \quad (39)$$

where

$$\mathbf{J}^{(s,1)} = e^2 \tau \int \frac{d^3 \mathbf{k}}{(2\pi)^3} (\nabla_{\mathbf{r}}\mu \times \boldsymbol{\Omega}_s) (\mathbf{v}^{(0,s)} \cdot \mathbf{E}) f'_0(\varepsilon_s), \quad \mathbf{J}^{(s,2)} = -e^2 \tau \int \frac{d^3 \mathbf{k}}{(2\pi)^3} \mathbf{v}^{(0,s)} [(\mathbf{E} \times \boldsymbol{\Omega}_s) \cdot \nabla_{\mathbf{r}}\mu] f'_0(\varepsilon_s), \quad (40)$$

$$\vartheta_{abc}^{(s,1)} = e^2 \tau \sum_d \epsilon_{abd} t_{cd}^s, \quad \vartheta_{abc}^{(s,2)} = -e^2 \tau \sum_d \epsilon_{bcd} t_{ad}^s, \quad \text{and} \quad t_{ab}^s = \int \frac{d^3 \mathbf{k}}{(2\pi)^3} v_a^{(0,s)} (\Omega_s)_b f'_0(\varepsilon_s). \quad (41)$$

We would like to point out that a term arising from $\nabla_{\mathbf{r}}\mu$ was missed in Ref. [30], as noted in our earlier work [19].

To express some of the above coefficients in a compact way, let us define the second-rank Berry-curvature tensor (BCD) [43],

$$D_{ab}^s = -\epsilon_{ab} \int_k \partial_a f_0(\varepsilon_s) (\Omega_s)_b = -\epsilon_{ab} t_{ab}^s. \quad (42)$$

It captures the dipole-moment of the BC over the occupied state. We will find that, in certain cases, the nonzero components of D_{ab}^s will be related to those of the ϑ 's.

A. Vortex nodal-ring

All the nonlinear-response coefficients evaluate to zero for an untilted VNR. For the tilted ones, we discuss two distinct cases: $\boldsymbol{\eta} = \eta_x \hat{\mathbf{x}}$ and $\boldsymbol{\eta} = \eta_z \hat{\mathbf{z}}$.

1. Case I: Tilt with respect to k_x -axis

The antisymmetric tensor D_{ab}^s [cf. Eq. (42)] evaluates to a nonzero value only for a nonzero tilt along the $k_x k_y$ -plane, which we choose to be $\eta_x \hat{\mathbf{x}}$. In particular, only D_{zx}^s and t_{zx}^s survive for a nonzero η_x . For $\boldsymbol{\eta} = \eta_x \hat{\mathbf{x}}$, $\eta_x > 0$, and $\mu \geq 0$, we obtain

$$D_{zx}^2 = \begin{cases} -\frac{1}{8\pi\eta_x} + \frac{\eta_x^2 K(\eta_x^2) - K(\eta_x^2) + E(\eta_x^2)}{2\pi^2\eta_x^3} & \text{for } \mu \geq \tilde{\eta} \\ -\frac{1}{8\pi\eta_x} + \frac{\sqrt{\tilde{\eta}^2 - \mu^2} (\sqrt{\tilde{\eta}^2 - \mu^2} \eta_x^2 - \tilde{\eta})}{4\pi^2\mu\tilde{\eta}\eta_x^3} + \frac{\cos^{-1}(\frac{\mu}{\tilde{\eta}})}{8\pi^2\eta_x} + \frac{E(\sin^{-1}(\frac{\mu\eta_x}{\tilde{\eta}})|\eta_x^{-2}) + E(\sin^{-1}\eta_x|\eta_x^{-2})}{4\pi^2\eta_x^2} & \text{for } \mu < \tilde{\eta} \end{cases} \quad (43)$$

and

$$D_{zx}^1 = \begin{cases} 0 & \text{for } \mu \geq \tilde{\eta} \\ \frac{\sqrt{\tilde{\eta}^2 - \mu^2}}{4\pi^2 \mu \eta_x^3} - \frac{\cos^{-1}(\frac{\mu}{\tilde{\eta}})}{8\pi^2 \eta_x} - \frac{\sqrt{(\tilde{\eta}^2 - \mu^2)(\tilde{\eta}^2 - \mu^2 \eta_x^2)}}{4\pi^2 \mu \tilde{\eta} \eta_x^3} + \frac{E(\sin^{-1} \eta_x | \eta_x^{-2}) - E(\sin^{-1}(\frac{\mu \eta_x}{\tilde{\eta}}) | \eta_x^{-2})}{4\pi^2 \eta_x^2} & \text{for } \mu < \tilde{\eta} \end{cases} \quad (44)$$

The second case for each band includes the scenarios with $\mu = 0$. Here, $K(\varphi)$ and $E(\varphi)$ give the complete elliptic integrals of the first and second kinds, respectively. Similarly, $F(\varphi; m)$ and $E(\varphi; m)$ denote the incomplete elliptic integrals of the first and second kinds, respectively. Also, for the second case, we need to compute the sum $(D_{zx}^1 + D_{zx}^2)$ as both the bands contribute for a given μ . For checking the limit of $\eta_x \rightarrow 0$ (as we approach it from the side of the band with $s = 1$), we must take the expression for D_{zx}^2 with $\mu \geq \tilde{\eta}$ — this gives $\eta_x/(64\pi)$ as the leading term. Thus, has a smooth limit for $\eta_x \rightarrow 0$ when it vanishes exactly at $\eta_x = 0$.

All the diagonal components, which are proportional to $\{t_{aa}^s\}$, vanish. Feeding the above into Eq. (41), we find that the nonzero components are captured by

$$\vartheta_{yzz}^{(s,1)} = -\vartheta_{zyz}^{(s,1)} = e^2 \tau D_{zx}^s, \quad \vartheta_{zxy}^{(s,2)} = -\vartheta_{zyx}^{(s,2)} = -e^2 \tau D_{zx}^s. \quad (45)$$

2. Case II: Tilt with respect to k_z -axis

For a nonzero tilt with respect to the k_z -axis, setting $\boldsymbol{\eta} = \eta_z \hat{\mathbf{z}}$, we find that only the diagonal terms, viz. $\{t_{aa}^s\}$, survive. In this scenario, there is no horn-cyclide formation and, for $\mu > 0$, only the $s = 2$ band contributes. We obtain

$$t_{xx}^2 = t_{yy}^2 = -\frac{t_{zz}^3}{2} = \frac{\eta_z^2 + 2\sqrt{1 - \eta_z^2} - 2}{16\pi \eta_z^3}. \quad (46)$$

Intriguingly, these are completely independent of the magnitude of μ , and has a smooth limit for $\eta_z \rightarrow 0$ when they vanish exactly at $\eta_z = 0$. This behaviour is similar to the features observed in Ref. [19], where a node with a nonzero BC-monopole was considered. Finally, we list the nonzero components as follows:

$$\vartheta_{abc}^{(s,1)} = e^2 \tau \epsilon_{abc} t_{cc}^s, \quad \vartheta_{abc}^{(s,2)} = -e^2 \tau \epsilon_{abc} t_{aa}^s. \quad (47)$$

B. \mathcal{PT} -symmetric nodal-ring

Analogous to the VNR case, an untilted PTNR too have vanishing nonlinear-response coefficients. Hence, we discuss the tilted scenarios with $\boldsymbol{\eta} = \eta_x \hat{\mathbf{x}}$ and $\boldsymbol{\eta} = \eta_z \hat{\mathbf{z}}$.

1. Case I: Tilt with respect to k_x -axis

No diagonal components, viz. $\{t_{aa}^s\}$, survive. There is a nonzero nonlinear response only for the D_{xy}^s -component of the BCD. This can be seen by starting with

$$D_{ab}^s = -\delta_{ax} \delta_{by} v_0 \eta_x \int \frac{d^3 \mathbf{k}}{(2\pi)^3} (\Omega_s)_y f'_0(\varepsilon_s). \quad (48)$$

Setting $\mu \geq 0$, the $s = 2$ band contributes with

$$\begin{aligned} D_{xy}^2 &= -\pi v_0 \eta_x \int \frac{d^3 \mathbf{k}}{(2\pi)^3} \cos \phi \delta(k_z) \delta(k_\perp - k_0) \delta(\tilde{\eta} \cos \phi - \mu) = \frac{-1}{(2\pi)^2} \int_{-1}^{\min[1, \mu/\tilde{\eta}]} \frac{du u}{\sqrt{1 - u^2}} \delta\left(u - \frac{\mu}{\tilde{\eta}}\right) \\ &= \frac{-1}{(2\pi)^2} \frac{\mu}{\sqrt{\tilde{\eta}^2 - \mu^2}} \Theta(1 - \mu/\tilde{\eta}), \end{aligned} \quad (49)$$

which is nonzero only if $\mu/\tilde{\eta} \leq 1$. The $s = 1$ band also contributes, whose value is

$$D_{xy}^1 = \frac{1}{(2\pi)^2} \int_{\mu/\tilde{\eta}}^1 \frac{du u}{\sqrt{1 - u^2}} \delta\left(u - \frac{\mu}{\tilde{\eta}}\right) \Theta(1 - \mu/\tilde{\eta}) = \frac{1}{(2\pi)^2} \frac{\mu}{\sqrt{\tilde{\eta}^2 - \mu^2}} \Theta(1 - \mu/\tilde{\eta}). \quad (50)$$

However, if we add up the two contribute, the net value is zero.

Using Eq. (14) at $T = 0$, we find that

$$\begin{aligned} \frac{J_x^{(s,1)}}{e^2 \tau} &= (-1)^s \pi \partial_x \mu \int \frac{d^3 \mathbf{k}}{(2\pi)^3} \cos \phi \delta(k_z) \delta(k_{\perp} - k_0) v_0 \eta_x E_x \delta(\tilde{\eta} \cos \phi - \mu) = -\partial_x \mu E_x D_{xy}^s, \\ \frac{J_y^{(s,1)}}{e^2 \tau} &= (-1)^s \pi \partial_y \mu \int \frac{d^3 \mathbf{k}}{(2\pi)^3} \sin \phi \delta(k_z) \delta(k_{\perp} - k_0) v_0 \eta_x E_x \delta(\tilde{\eta} \cos \phi - \mu) = 0, \\ \frac{J_z^{(s,1)}}{e^2 \tau} &= -(-1)^s \pi \int \frac{d^3 \mathbf{k}}{(2\pi)^3} (\partial_x \mu \cos \phi + \partial_y \mu \sin \phi) \delta(k_z) \delta(k_{\perp} - k_0) v_0 \eta_x E_x \delta(\tilde{\eta} \cos \phi - \mu) = \partial_x \mu E_x D_{xy}^s. \end{aligned} \quad (51)$$

Now, for $\mathbf{J}^{(s,2)}$, only the x -component survives, which evaluates to

$$\begin{aligned} \frac{J_x^{(s,2)}}{e^2 \tau} &= -(-1)^s \pi v_0 \eta_x \int \frac{d^3 \mathbf{k}}{(2\pi)^3} \delta(k_z) \delta(k_{\perp} - k_0) [\partial_x \mu E_z \cos \phi + \partial_y \mu E_z \sin \phi - \partial_z \mu (E_x \cos \phi + E_y \sin \phi)] \delta(\tilde{\eta} \cos \phi - \mu) \\ &= (\partial_x \mu E_z - \partial_z \mu E_x) D_{xy}^s. \end{aligned} \quad (52)$$

From the above expressions, we can easily infer that the only nonzero coefficients are captured by

$$-\vartheta_{xxx}^{(s,1)} = \vartheta_{zxx}^{(s,1)} = \vartheta_{xxz}^{(s,2)} = -\vartheta_{xzx}^{(s,2)} = e^2 \tau D_{xy}^s. \quad (53)$$

2. Case II: Tilt with respect to k_z -axis

A nonzero tilt $\boldsymbol{\eta} = \eta_z \hat{z}$ does not give any nonzero nonlinear response.

C. Three-band Hopf semimetal

For the BC-dipole nodal point, keeping with the trend of the nodal-ring systems, there is zero linear response for no tilt. Therefore, we will consider the two cases: $\boldsymbol{\eta} = \eta_x \hat{x}$ and $\boldsymbol{\eta} = \eta_z \hat{z}$.

1. Case I: Tilt with respect to k_x -axis

In analogy with the VNR and PTNR casea, all diagonal components, viz. $\{t_{aa}^s\}$, vanish. As for the off-diagonal components proportional to the BCD, only those $\propto D_{zx}^s$ survive just like the VNR system. Explicit calculations lead to

$$D_{zx}^s = \frac{\eta_x (2\eta_x^2 - 3) + 3(1 - \eta_x^2) \tanh^{-1} \eta_x}{12\pi^2 \eta_x^4} \quad \text{for } s = 1 \text{ and } s = 2. \quad (54)$$

Intriguingly, the results are completely independent of μ . Eq. (45) is applicable due to the similarities in the surviving terms. The $\eta_x \rightarrow 0$ limit is smooth, with the answer being $-\eta_x/(30\pi^2) + \mathcal{O}(\eta_x^2)$.

2. Case II: Tilt with respect to k_z -axis

Again, agreeing with the VNR results, we get a nonzero answer for the diagonal components $\propto t_{aa}^s$, while all the off-diagonal components proportional to the BCD vanish. For the diagonal ones, we get

$$t_{xx}^s = t_{yy}^s = \frac{\eta_z {}_2F_1(1, \frac{3}{2}; \frac{7}{2}; \eta_z^2)}{30\pi^2} \quad \text{and} \quad t_{zz}^s = \frac{\eta_z (2\eta_z^2 - 3) + 3(1 - \eta_z^2) \tanh^{-1} \eta_z}{6\pi^2 \eta_z^4} \quad \text{for } s = 1 \text{ and } s = 2. \quad (55)$$

Here, ${}_2F_1(a, b; c; z)$ is the Gaussian or ordinary hypergeometric function. Again, the results are completely independent of μ and has a smooth limit for $\eta_z \rightarrow 0$ (vanishing exactly at $\eta_z = 0$). Eq. (47) is applicable to get the final forms of the three-index tensors.

V. SUMMARY AND OUTLOOK

In this paper, we have focussed on bringing out some unique features of exotic semimetals in the forms of VNR, PTNR, and 3-band BC-dipole, as reflected in longitudinal magnetoconductivity (σ_{zz}) and the ECR. While nodal-rings intrinsically possess isotropic dispersions (due to their toroidal-shaped Fermi surfaces), the BC-dipole nodal point has a spherical Fermi surface and an isotropic Fermi surface. Nevertheless, both kinds of systems display anisotropic response [44] due to their BC being anisotropic. In particular, if we analyse the BC-profiles of the VNR and the BC-dipole, dipole-like sources are revealed [cf. Fig. 2]. Thus, these two systems show some qualitative similarities in both the linear and nonlinear response-coefficients investigated in this paper. Intriguingly, our results bring out the crucial role of topology in causing the intrinsic anisotropy, despite the dispersion being perfectly isotropic, which in turn makes the response different from a truly isotropic system (i.e., ones with isotropic BC-profiles). It is important to note that σ_{zz} shows linear-in- $|\mathbf{B}|$ dependence, in addition to the usual quadratic-in- $|\mathbf{B}|$ dependence of isotropic nodal-point semimetals [21, 45]. This is because the dipole-like anisotropies in the BC allow to satisfy the Onsager-Casimir reciprocity relations [46–48], making the linear-in- $|\mathbf{B}|$ terms survive. In the future, it will be worthwhile to repeat our calculations for a magnetic field which is not exactly collinear with the electric field [49]. The resulting nonzero components of conductivity in the form of Hall and planar-Hall response will be another feature which will serve as an important signature to be probed in transport-experiments.

APPENDIX: LIMITS OF ANGULAR INTEGRALS FOR TILTED NODAL-RINGS

Clearly, if $\mu < \tilde{\eta}$, we have to restrict the upper (lower) limit of $\cos\phi$ to $\mu/\tilde{\eta}$ for the $s = 2$ ($s = 1$) band. Overall, let us spell out the step-by-step strategy when we apply a chemical potential $\mu \geq 0$:

1. Implementing the Dirac-delta function, we get rid of the κ -integral and replace κ by $(\mu - \tilde{\eta} \cos\phi)/(v_0 \zeta_s)$ in the integrand. Say, the integral is now $I_s = \int_0^{2\pi} d\gamma \int_{-\pi}^{\pi} d\phi \mathcal{I}_s(\gamma, \phi)$.
2. Perform the γ -integral first to get the form $I_s = \int_{-\pi}^{\pi} d\phi \tilde{\mathcal{I}}_s(\gamma, \phi)$.
3. We divide up the integral as $I_s = I_1^{(s)} + I_2^{(s)}$, where $I_1^{(s)} = \int_{-\pi}^{-\phi_m} d\phi \tilde{\mathcal{I}}_s(\phi)$, $I_2^{(s)} = \int_{\phi_m}^{\pi} d\phi \tilde{\mathcal{I}}_s(\phi)$, and $\phi_m = \max[0, \cos^{-1}(\mu/\tilde{\eta})]$. If $\tilde{\mathcal{I}}_s(\phi)$ is even (odd) in ϕ , then $I_s = 2I_2^{(s)}$ ($I_s = 0$).
4. Set $s = 2$ and change variables as $u = \cos\phi$, which lead to $I_2^{(2)} = \int_{-1}^0 \frac{du}{\sqrt{1-u^2}} \tilde{\mathcal{I}}_2(\cos^{-1} u) + \int_0^{u_m} \frac{du}{\sqrt{1-u^2}} \tilde{\mathcal{I}}_2(\cos^{-1} u)$, where u_m is the upper limit determined by $\min[1, \mu/\tilde{\eta}]$.
5. If $\mu < \tilde{\eta}$, a section of the $s = 1$ band is cut by $\mu \geq 0$ as well, and the conductivity gets contributions both from $s = 1$ and $s = 2$. For the $s = 1$ band, we need to employ a strategy similar to the $s = 2$ band, using the appropriate limits for the ϕ -integrals.

-
- [1] A. A. Burkov and L. Balents, Weyl semimetal in a topological insulator multilayer, *Phys. Rev. Lett.* **107**, 127205 (2011).
[2] B. Yan and C. Felser, Topological materials: Weyl semimetals, *Annual Rev. of Condensed Matter Phys.* **8**, 337 (2017).
[3] B. Bradlyn, J. Cano, Z. Wang, M. G. Vergniory, C. Felser, R. J. Cava, and B. A. Bernevig, Beyond Dirac and Weyl fermions: Unconventional quasiparticles in conventional crystals, *Science* **353** (2016).
[4] F. Flicker, F. de Juan, B. Bradlyn, T. Morimoto, M. G. Vergniory, and A. G. Grushin, Chiral optical response of multifold fermions, *Phys. Rev. B* **98**, 155145 (2018).
[5] A. A. Burkov, M. D. Hook, and L. Balents, Topological nodal semimetals, *Phys. Rev. B* **84**, 235126 (2011).
[6] L.-K. Lim and R. Moessner, Pseudospin vortex ring with a nodal line in three dimensions, *Phys. Rev. Lett.* **118**, 016401 (2017).
[7] D. Xiao, M.-C. Chang, and Q. Niu, Berry phase effects on electronic properties, *Rev. Mod. Phys.* **82**, 1959 (2010); G. Sundaram and Q. Niu, Wave-packet dynamics in slowly perturbed crystals: Gradient corrections and Berry-phase effects, *Phys. Rev. B* **59**, 14915 (1999).
[8] A. Graf and F. Piéchon, Berry curvature and quantum metric in N -band systems: An eigenprojector approach, *Phys. Rev. B* **104**, 085114 (2021); A. Graf, *Aspects of multiband systems: Quantum geometry, flat bands, and multifold fermions*, Theses, Université Paris-Saclay (2022).
[9] F. D. M. Haldane, Berry curvature on the Fermi surface: Anomalous Hall effect as a topological Fermi-liquid property, *Phys. Rev. Lett.* **93**, 206602 (2004).
[10] P. Goswami and S. Tewari, Axionic field theory of $(3+1)$ -dimensional Weyl semimetals, *Phys. Rev. B* **88**, 245107 (2013).
[11] A. A. Burkov, Anomalous Hall effect in Weyl metals, *Phys. Rev. Lett.* **113**, 187202 (2014).
[12] S.-B. Zhang, H.-Z. Lu, and S.-Q. Shen, Linear magnetoconductivity in an intrinsic topological Weyl semimetal, *New Journal of Phys.* **18**, 053039 (2016).
[13] Q. Chen and G. A. Fiete, Thermoelectric transport in double-Weyl semimetals, *Phys. Rev. B* **93**, 155125 (2016).

- [14] S. Nandy, G. Sharma, A. Taraphder, and S. Tewari, Chiral anomaly as the origin of the planar Hall effect in Weyl semimetals, *Phys. Rev. Lett.* **119**, 176804 (2017); S. Nandy, A. Taraphder, and S. Tewari, Berry phase theory of planar Hall effect in topological insulators, *Scientific Reports* **8**, 14983 (2018); I. Mandal, Effects of time-periodic drive in the linear response for planar-Hall set-ups with Weyl and multi-Weyl semimetals, *Canadian Journal of Physics* **103**, 1147 (2025).
- [15] K. Das and A. Agarwal, Linear magnetochiral transport in tilted type-I and type-II Weyl semimetals, *Phys. Rev. B* **99**, 085405 (2019); Thermal and gravitational chiral anomaly induced magneto-transport in Weyl semimetals, *Phys. Rev. Res.* **2**, 013088 (2020).
- [16] I. Mandal and K. Saha, Thermoelectric response in nodal-point semimetals, *Ann. Phys. (Berlin)* **536**, 2400016 (2024).
- [17] L. Medel, R. Ghosh, A. Martín-Ruiz, and I. Mandal, Electric, thermal, and thermoelectric magnetoconductivity for Weyl/multi-Weyl semimetals in planar Hall set-ups induced by the combined effects of topology and strain, *Scientific Reports* **14**, 21390 (2024); I. Mandal, Anisotropic conductivity for the type-I and type-II phases of Weyl/multi-Weyl semimetals in planar Hall set-ups, *Annals of Physics* **482**, 170181 (2025).
- [18] R. Ghosh, F. Haidar, and I. Mandal, Linear response in planar Hall and thermal Hall setups for Rarita-Schwinger-Weyl semimetals, *Phys. Rev. B* **110**, 245113 (2024).
- [19] I. Mandal, S. Saha, and R. Ghosh, Signatures of topology in generic transport measurements for Rarita-Schwinger-Weyl semimetals, *Solid State Communications* **397**, 115799 (2025).
- [20] F. Haidar and I. Mandal, Reflections of topological properties in the planar-Hall response for semimetals carrying pseudospin-1 quantum numbers, *Annals of Physics* **478**, 170010 (2025).
- [21] A. Knoll, C. Timm, and T. Meng, Negative longitudinal magnetoconductance at weak fields in Weyl semimetals, *Phys. Rev. B* **101**, 201402 (2020); I. Mandal, Longitudinal magnetoconductivity in multifold semimetals exemplified by pseudospin-1 nodal points, *Eur. Phys. J. Plus* **141**, 75 (2026); I. Mandal, Distinguishing features of longitudinal magnetoconductivity for a Rarita-Schwinger-Weyl node, *arXiv e-prints* (2025), arXiv:2506.12380 [cond-mat.mes-hall].
- [22] I. Mandal, Disentangling contributions to longitudinal magnetoconductivity for Kramers-Weyl nodes, *Sci. Rep.* **15**, 37542 (2025).
- [23] L. Li, J. Cao, C. Cui, Z.-M. Yu, and Y. Yao, Planar Hall effect in topological Weyl and nodal-line semimetals, *Phys. Rev. B* **108**, 085120 (2023).
- [24] F. Hussain Rather, M. Jaffar A., and I. Mandal, Direction-dependent linear response for gapped nodal-line semimetals in planar-Hall configurations, *arXiv e-prints* (2025), arXiv:2503.10712 [cond-mat.mes-hall].
- [25] W. B. Rui, Y. X. Zhao, and A. P. Schnyder, Topological transport in Dirac nodal-line semimetals, *Phys. Rev. B* **97**, 161113 (2018).
- [26] M.-X. Yang, H. Geng, W. Luo, L. Sheng, W. Chen, and D. Y. Xing, Sign reversal of magnetoresistivity in massive nodal-line semimetals due to the Lifshitz transition of the Fermi surface, *Phys. Rev. B* **104**, 165149 (2021).
- [27] W. L. Min-Xue Yang and W. Chen, Quantum transport in topological nodal-line semimetals, *Advances in Physics: X* **7**, 2065216 (2022).
- [28] M. N. Chen, W. C. Chen, and Y. Zhou, Topological hybrid semimetal phases and anomalous Hall effects in a three dimensional magnetic topological insulator, *Journal of Physics: Condensed Matter* **34**, 025502 (2021).
- [29] S. Sekh and I. Mandal, Magnus Hall effect in three-dimensional topological semimetals, *Eur. Phys. J. Plus* **137**, 736 (2022).
- [30] R. Flores-Calderón, L. Medel, and A. Martín-Ruiz, Electrochemical transport in Dirac nodal-line semimetals, *EPL (Europhysics Letters)* **143**, 16001 (2023).
- [31] J. Noky, Q. Xu, C. Felser, and Y. Sun, Large anomalous Hall and Nernst effects from nodal line symmetry breaking in Fe_2MnX ($\text{X} = \text{P}, \text{As}, \text{Sb}$), *Phys. Rev. B* **99**, 165117 (2019).
- [32] E. Liu, Y. Sun, N. Kumar, L. Muechler, A. Sun, L. Jiao, S.-Y. Yang, D. Liu, A. Liang, Q. Xu, J. Kroder, V. Süß, H. Borrmann, C. Shekhar, Z. Wang, C. Xi, W. Wang, W. Schnelle, S. Wirth, Y. Chen, S. T. B. Goennenwein, and C. Felser, Giant anomalous Hall effect in a ferromagnetic Kagome-lattice semimetal, *Nature Physics* **14**, 1125 (2018).
- [33] B. Yang, Y. Bi, R.-X. Zhang, R.-Y. Zhang, O. You, Z. Zhu, J. Feng, H. Sun, C. T. Chan, C.-X. Liu, and S. Zhang, Momentum space toroidal moment in a photonic metamaterial, *Nature Communications* **12**, 1784 (2021).
- [34] Q. Wu, A. A. Soluyanov, and T. Bzdušek, Non-abelian band topology in noninteracting metals, *Science* **365**, 1273 (2019).
- [35] A. Graf and F. Piéchon, Massless multifold Hopf semimetals, *Phys. Rev. B* **108**, 115105 (2023).
- [36] T. Habe, Optical conductivity of the threefold Hopf semimetal, *Phys. Rev. B* **106**, 205204 (2022); S. Ahn, Magneto-optical conductivity of threefold Hopf semimetals, *Journal of the Korean Physical Society* **84**, 59 (2024).
- [37] I. Mandal, Fermi arcs for generic nodal points hosting monopoles or dipoles, *arXiv e-prints* (2025), arXiv:2510.18785 [cond-mat.mes-hall].
- [38] W. Chen, H.-Z. Lu, and O. Zilberberg, Weak localization and antilocalization in nodal-line semimetals: Dimensionality and topological effects, *Phys. Rev. Lett.* **122**, 196603 (2019).
- [39] S. Ahn, E. J. Mele, and H. Min, Electrodynamics on Fermi cyclides in nodal line semimetals, *Phys. Rev. Lett.* **119**, 147402 (2017).
- [40] J. N. Fuchs, F. Piéchon, M. O. Goerbig, and G. Montambaux, Topological Berry phase and semiclassical quantization of cyclotron orbits for two dimensional electrons in coupled band models, *Eur. Phys. J. Plus* **77**, 351 (2010).
- [41] N. Ashcroft and N. Mermin, *Solid State Physics* (Cengage Learning, 2011).
- [42] L. Li, J. Cao, C. Cui, Z.-M. Yu, and Y. Yao, Planar hall effect in topological Weyl and nodal-line semimetals, *Phys. Rev. B* **108**, 085120 (2023).
- [43] I. Sodemann and L. Fu, Quantum nonlinear Hall effect induced by Berry curvature dipole in time-reversal invariant materials, *Phys. Rev. Lett.* **115**, 216806 (2015).
- [44] S. Ahn, Anisotropic plasmons in threefold hopf semimetals, *Europhysics Letters* **149**, 16001 (2025).
- [45] I. Mandal, Chiral anomaly and internode scatterings in multifold semimetals, *Phys. Rev. B* **111**, 165116 (2025).
- [46] L. Onsager, Reciprocal Relations in Irreversible Processes. I., *Phys. Rev.* **37**, 405 (1931).
- [47] H. B. G. Casimir, On Onsager's principle of microscopic reversibility, *Rev. Mod. Phys.* **17**, 343 (1945).

- [48] P. Jacquod, R. S. Whitney, J. Meair, and M. Büttiker, Onsager relations in coupled electric, thermoelectric, and spin transport: The tenfold way, *Phys. Rev. B* **86**, 155118 (2012).
- [49] A. Ahmad, K. V. Raman, S. Tewari, and G. Sharma, Longitudinal magnetoconductance and the planar Hall conductance in inhomogeneous Weyl semimetals, *Phys. Rev. B* **107**, 144206 (2023).